



## 2D simulation and performance evaluation of bifacial rear local contact c-Si solar cells under variable illumination conditions

Item Type	Article
Authors	Katsaounis, Theodoros;Kotsovos, Konstantinos;Gereige, Issam;Al-Saggaf, Ahmed;Tzavaras, Athanasios
Citation	Katsaounis T, Kotsovos K, Gereige I, Al-Saggaf A, Tzavaras A (2017) 2D simulation and performance evaluation of bifacial rear local contact c-Si solar cells under variable illumination conditions. Solar Energy 158: 34–41. Available: <a href="http://dx.doi.org/10.1016/j.solener.2017.09.023">http://dx.doi.org/10.1016/j.solener.2017.09.023</a> .
Eprint version	Post-print
DOI	<a href="https://doi.org/10.1016/j.solener.2017.09.023">10.1016/j.solener.2017.09.023</a>
Publisher	Elsevier BV
Journal	Solar Energy
Rights	NOTICE: this is the author's version of a work that was accepted for publication in Solar Energy. Changes resulting from the publishing process, such as peer review, editing, corrections, structural formatting, and other quality control mechanisms may not be reflected in this document. Changes may have been made to this work since it was submitted for publication. A definitive version was subsequently published in Solar Energy, [ , [2017-09-23]] DOI: 10.1016/j.solener.2017.09.023 . © 2017. This manuscript version is made available under the CC-BY-NC-ND 4.0 license <a href="http://creativecommons.org/licenses/by-nc-nd/4.0/">http://creativecommons.org/licenses/by-nc-nd/4.0/</a>
Download date	2025-06-18 12:53:23
Link to Item	<a href="http://hdl.handle.net/10754/625470">http://hdl.handle.net/10754/625470</a>

# 2D simulation and performance evaluation of bifacial high efficiency c-Si solar cells under variable illumination conditions

Th. Katsaounis <sup>\*1,3</sup>, K. Kotsovos <sup>†2</sup>, I. Gereige <sup>2</sup>, A. Al-Saggaf <sup>2</sup>, and A. Tzavaras <sup>1</sup>

<sup>1</sup>Computer Electrical and Mathematical Science & Engineering (CEMSE), KAUST,  
Thuwal Saudi Arabia

<sup>2</sup>Renewable Energy — Carbon Management Division, Saudi Aramco, Thuwal Saudi  
Arabia

<sup>3</sup>IACM, FORTH, Heraklion, Greece

September 18, 2017

## Abstract

A customized 2D computational tool has been developed to simulate bifacial rear local contact PERC type PV structures based on the numerical solution of the transport equations through the finite element method. Simulations were performed under various device material parameters and back contact geometry configurations in order to optimize bifacial solar cell performance under different simulated illumination conditions. Bifacial device maximum power output was also compared with the monofacial equivalent one and the industrial standard Al-BSF structure. The performance of the bifacial structure during highly diffused irradiance conditions commonly observed in the Middle East region due to high concentrations of airborne dust particles was also investigated. Simulation results demonstrated that such conditions are highly favorable for the bifacial device because of the significantly increased diffuse component of the solar radiation which enters the back cell surface.

## 1 Introduction

Bifacial solar cells have recently gained attention in the PV market since they provide increased energy yield compared to conventional monofacial modules due to additional light absorbed through the back surface [1], [2], [3]. Although bifacial PV technologies were developed some decades ago [4], [5], their manufacturing process at that time was quite complicated, making them unfavourable for mass production. However, during the last few years, advances in industrial processes have been implemented to reduce the cost of bifacial PV modules and various companies have introduced such products [6], [7], [8], [9], therefore their market share is predicted to increase significantly in the near future [10]. In addition, high efficiency solar cell structures, like the passivated emitter and rear cell with local passivated contacts (PERC) [11], or the passivated emitter, rear locally diffused cell (PERL) [12], can potentially offer improved conversion efficiencies and higher yield compared to the industrial standard Al-BSF (aluminium back surface field) in bifacial configuration.

Although performance simulation and energy yield calculation are very common and straightforward in commercial PV software, modelling of bifacial module performance is challenging due to the variable illumination conditions on the back surface which depend on different parameters, such as the percentage of diffuse radiation in the solar spectrum, ground reflectance, module elevation angle, orientation and tilt angle [1]. In this regard, the development of a simulation model that could take into account the different illumination conditions and also provide guidelines to an optimized solar cell structure based on various material parameters and design configuration is important. There are currently various PV device simulators, which can solve the solar cell transport equations in 2 or 3 dimensions [13], [14], [15],

---

\*theodoros.katsaounis@kaust.edu.sa

†konstantinos.kotsovos@aramco.com

[16], which have been widely used to simulate high efficiency 3D structures including the PERC/PERL [17], [18] and interdigitated back contact (IBC) solar cells [19], [20]. Simulation of bifacial solar cell structures is possible with some of these simulators [21], [22], [23],[24] and already implemented in 2D, however their input parameters such as geometry, light trapping and photogeneration profile need to be specially configured to account for front and rear side illumination.

Our approach in this work is the development of a customized 2D computational tool specifically tailored for bifacial PV structures similar to PERC/PERL for providing guidelines towards optimizing bifacial solar cell design parameters in terms of efficiency and simulate the various illumination conditions observed for such types of modules. Such a tool will allow us to have complete control on the mathematical model being used as well as the numerical method applied to solve it. Industrial solvers can rarely provide such a versatility. The formulation of the model is similar with the one developed in [25]. We introduce a novel change of variables which transforms the transport equations to a dimensionless system, thus facilitating considerably its numerical approximation. Another novel feature that our solver possesses is mesh adaptivity, which allows to resolve accurately and efficiently the localized nature of the incident light on the surface and high gradient variations of the solution in the neighbourhood of the contact.

The solution of the transport equations is obtained through the finite element method, as described in section 2. Simulation results are presented in section 3, where various device configurations are considered by varying the rear contact geometry, base substrate material parameters as well as different illumination conditions for the bifacial structure and comparing its maximum power output performance with the monofacial equivalent device. Section 4 is investigating the performance of the optimized bifacial structure based on the results of section 3, and considering variations of the solar spectrum due to light scattering by dust particles, which is commonly observed in Middle East area. Finally, section 5 discusses the main conclusions of this work.

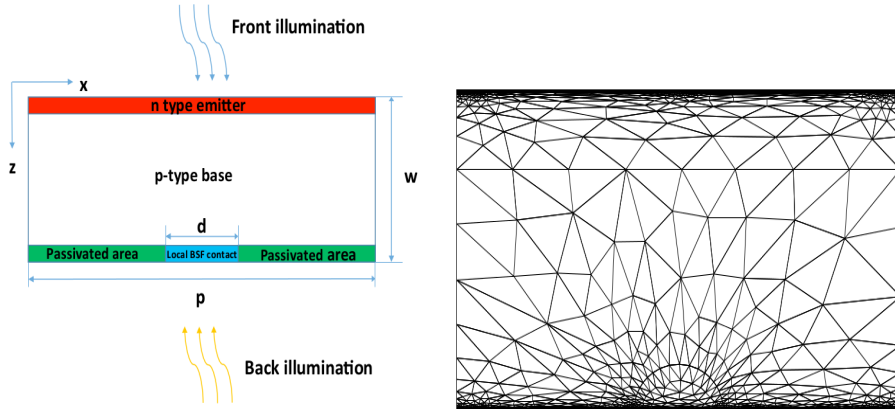


Figure 1: Geometry of solar device (left) and a representative triangulation (right)

## 2 The mathematical model

Throughout this work we assume that the solar cell device operates in a low injection and steady state regime. In this regime the classical drift-diffusion equations can be simplified and the system decouples since current transport is dominated by diffusion. The continuity equation for the minority (electron) carrier concentration  $n(x, z)$  and the voltage drop  $V(x, z)$  in this regime, are given by, [25]

$$\begin{aligned} \Delta n &= \frac{1}{D_n} \left( \frac{n}{\tau_n} - G \right), & (x, z) \in [0, p] \times [0, w], \\ \Delta V &= \left( \frac{n}{\tau_n} - G \right) \left( \frac{D_n - D_p}{\mu_p N_A D_n} \right), & (x, z) \in [0, p] \times [0, w], \end{aligned} \quad (1)$$

where  $\tau_n$  is the minority carrier lifetime,  $D_n, D_p$  are the diffusivity constants of minority and majority carriers respectively,  $\mu_p$  is the majority carrier mobility,  $N_A$  is the hole doping density, while  $G(x, z)$

denotes the generation rate. A sketch of the device under consideration is shown in Figure 1(left). The above system is augmented with the following set of boundary conditions:

- Vertical sides:  $x = 0, L, z \in (0, w)$ ,

$$\nabla n \cdot \zeta = 0, \quad \nabla V \cdot \zeta = 0. \quad (2)$$

- Top side:  $z = 0, x \in (0, L)$ ,

$$n = \frac{n_i^2}{N_A} \left( \exp \left( \frac{V_{bias} + V}{V_T} \right) - 1 \right), \quad -q D_p \nabla n \cdot \zeta = -J_0 \left( \exp \left( \frac{V_{bias} + V}{V_T} \right) - 1 \right). \quad (3)$$

- Bottom side :  $z = w, x \in (0, L)$ ,

$$\begin{aligned} D_n \nabla n \cdot \zeta &= -S n, \\ \text{outside contact : } \nabla V \cdot \zeta &= -n \frac{S_1(D_n - D_p)}{\mu_p N_A D_n}, \quad \text{inside contact : } V = 0, \end{aligned} \quad (4)$$

where  $\zeta$  is the outward normal to the side,  $q$  is the electron charge,  $V_T = \frac{kT}{q}$  is the thermal voltage,  $S$  is the recombination velocity with  $S = s_1$  outside the contact and  $S = s_2$  inside the contact. Further,  $n_i$  denotes the intrinsic carrier concentration,  $J_0$  the saturation current density and  $V_{bias}$  is the external applied voltage.

The multiscale and nonlinear nature of system (1)-(4) poses various computational challenges, when one attempts to approximate its solution numerically. First we introduce a novel change of variables that transforms system (1) to a non-dimensional one. The classical approach in this direction is to use the Debye length for scaling the space variables, the thermal voltage for the voltage drop and the intrinsic concentration for the minority carrier, [26], [27]. However in the current regime, where diffusion is the dominating factor, it is more appropriate to use more suitable quantities to scale the corresponding variables. In particular, we use the diffusion length to scale the space variables and a particular voltage to scale the related potentials:

$$\begin{aligned} x' &= \frac{x}{L_n}, \quad z' = \frac{z}{L_n}, \quad L_n = \sqrt{D_n \tau_n}, \\ n &= N_A \exp \left[ \frac{V - \phi_n}{V_T} \right], \quad \eta = \frac{n}{N_A}, \\ u &= \frac{V}{V_C}, \quad v = \frac{\phi_n}{V_C} \implies \eta = \exp \left( \frac{V_C}{V_T} (u - v) \right), \\ V_C &= \frac{D_n - D_p}{\mu_p} = V_T \left( \frac{\mu_n}{\mu_p} - 1 \right), \quad (\mu_n > \mu_p), \end{aligned} \quad (5)$$

where we assumed that  $n$  is expressed in terms of a quasi-Fermi potential  $\phi_n$ ,  $L_n$  is the diffusion length and  $V_C$  is multiple of the thermal voltage  $V_T$ . To the best of our knowledge this scaling of variables is new in the literature. Using this change of variables we derive a new system, which is dimensionless

$$\begin{aligned} -\Delta \eta + \eta &= g_n, \\ -\Delta u + \eta &= g_n, \end{aligned} \quad (6)$$

where  $g_n = G \frac{L_n^2}{N_A D_n}$ . The new form of the boundary conditions is

- Vertical sides:  $x = 0, L, z \in (0, w)$ ,

$$\nabla \eta \cdot \zeta = 0, \quad \nabla u \cdot \zeta = 0. \quad (7)$$

- Top side:  $z = 0, x \in (0, L)$ ,

$$\nu_A^2 \eta = \exp \left( \frac{V_C}{V_T} (V_b + u) \right) - 1, \quad \nabla u \cdot \zeta = \nu_A^2 j_0 \left( 1 - \exp \left( -\frac{V_C}{V_T} (V_b + u) \right) \right). \quad (8)$$

- Bottom side :  $z = w$ ,  $x \in (0, L)$ ,

$$\begin{aligned} \nabla \eta \cdot \zeta &= -s_n \eta, \\ \text{outside contact : } \nabla u \cdot \zeta &= -s_n \eta, \\ \text{inside contact : } u &= 0, \end{aligned} \tag{9}$$

where  $V_b = \frac{V_{bias}}{V_C}$ ,  $\nu_A = \frac{n_i}{N_A}$ ,  $j_0 = J_0 \frac{L_n}{qD_p N_A} \frac{V_T}{V_C}$  and  $s_n = S \frac{L_n}{D_n}$ .

## 2.1 The numerical method

We use the finite element method to solve numerically system (6)-(9). The implementation using finite elements was chosen because the FFT method used in [25] does not allow mesh adaptation, has slower convergence compared to finite element method and provides the solution only on the top and bottom surface of the device. The nonlinear nature of the system stems from the boundary conditions (7)-(9). Using the finite element framework we can incorporate these nonlinearities in the numerical method in a natural way. To solve the resulting system of nonlinear equations we use Newton's method. However, its direct application to the full system (6) would lead to a solution of a large linear system which is computationally very expensive. Instead, we use an *implicit - explicit* variant of Newton's method, which decouples the system and each equation is solved separately, [28]. System (6) can be written in the form

$$\mathcal{F}(\eta, u) = 0, \quad \mathcal{G}(\eta, u) = 0,$$

where  $\mathcal{F}, \mathcal{G}$  represent its finite element discretization given by the corresponding variational formulation. Then the iterative scheme works as follows : given an approximate  $(\eta_\ell, u_\ell)$  we compute the next iterate by solving

$$\mathcal{F}(\eta_{\ell+1}, u_\ell) = 0, \quad \mathcal{G}(\eta_{\ell+1}, u_{\ell+1}) = 0, \quad \ell = 0, \dots, \ell_m, \tag{10}$$

where the number of iterations  $\ell_m$  required for convergence depends mainly on the required accuracy. As an initial condition to the iterative scheme we take  $(\eta_0, u_0) = (0, 0)$ . Another issue we face numerically is related to the source term  $g_n$  in (6) which describes the incident light on cell's surface. Most of the incoming light is absorbed within few nanometers from the surface, which mathematically translates to the presence of a Dirac-like function supported in a small neighbourhood of the boundary. To resolve this issue numerically we rely on mesh adaptivity, in particular the initial mesh is locally adapted according to the variation of  $g_n$ , [29], see Figure 1(right). Mesh adaptation is performed also inside the iterative scheme to adjust mainly to the variation of  $(u, \eta)$  and capture their behaviour around the contact. Typically no more than two adaptive steps were required during the whole computation producing, on the average, a mesh of about 40K triangles and 18K degrees of freedom. We remark that failure to resolve the source term  $g_n$  adequately might lead to a completely wrong solution.

## 2.2 Comparison with existing solvers

Before presenting the main results, we briefly compare our numerical solver with two well known and publicly available solar cell simulators, namely with *Quokka*, [15] and *PC2D*, [16]. We limit the comparison only to single face solar devices since Quokka does not support bifacial structures at its current configuration, while PC2D can be extended to simulate bifacial illumination, but requires a work-around for setting the photogeneration rate. We consider a solar cell where the incident light operates only on the top surface, where a small portion of it is covered by a metallic grid, see Figure 2, and we have taken  $p = 1200\mu m$ ,  $w = 180\mu m$ ,  $d = 120\mu m$ ,  $L_n = 1200\mu m$ , while the size of the metallic grid is  $120\mu m$ . The emitter saturation current is  $J_0 = 10^{-13} A/cm^2$ , while at the back contact the recombination current is  $J_{0C} = 10^{-12} A/cm^2$ . We have also considered the optical losses due to reflection,

$$G = \int \alpha(\lambda)(1 - R(\lambda))I_G e^{-\alpha(\lambda)z} d\lambda$$

where the reflection distribution  $R(\lambda)$  was obtained using the resources in [30]. The rest of parameters used in the simulations are as in Section 3. In Table 1 we present the values of standard characteristic quantities in solar cells simulations based on the corresponding IV-curves computed by the three different

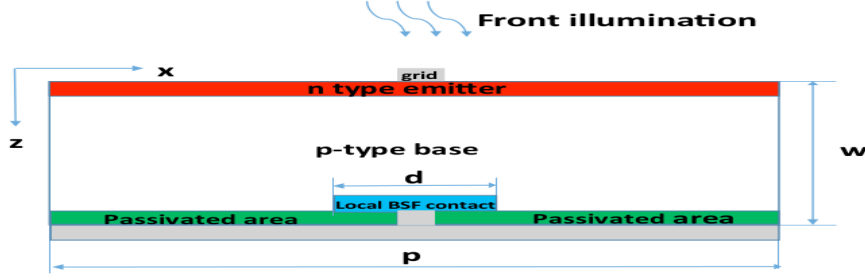


Figure 2: Single-face solar cell with metallic grid

solvers with *KASCS* being our solver. The values we compare include the *short circuit current* ( $J_{sc}$ ), the *open circuit voltage* ( $V_{oc}$ ), the *maximum power* ( $P_{mp}$ ) with the corresponding values of current  $J_{mp}$  and voltage  $V_{mp}$ , as well as the *fill factor* ( $FF$ ) and *efficiency* ( $Eff$ ). We also quantify the difference in the values of our solver and that of the other two in terms of the absolute (AD) and relative (RD) difference respectively. All three solvers produce comparable results and in most cases the corresponding relative

	KASCS	Quokka	AD	RD(%)	PC2D	AD	RD(%)
$J_{sc}(mA/cm^2)$	39.991	38.651	1.34	3.35	39.173	0.82	2.05
$V_{oc}(mV)$	651.425	664.079	12.65	1.94	664.000	12.58	1.93
$P_{mp}(mW/cm^2)$	21.776	21.369	0.41	1.87	21.653	0.12	0.56
$V_{mp}(mV)$	569.675	577.208	7.53	1.32	575.415	5.74	1.01
$J_{mp}(mA/cm^2)$	38.225	36.955	1.27	3.32	37.631	0.59	1.54
$FF$	83.588	83.106	0.48	0.58	83.377	0.21	0.25
$Eff(\%)$	21.776	21.369	0.41	1.87	21.653	0.12	0.56

Table 1: Comparison of characteristic values

differences are below 2%. However the differences in Table 1 can be attributed to : a) modelling assumptions: the simulators solve similar but not exactly the same system of transport equations and type of boundary conditions; b) solution method: KASCS and PC2D both use finite elements but PC2D utilises a very coarse grid, compared to the adaptive grid used in KASCS. On the other hand Quokka uses a finite volume method; c) photogeneration resolution: KASCS uses a highly adaptive grid to resolve the incident light, while PC2D and Quokka are using much coarser grids.

Finally, in Figure 3, we plotted the corresponding IV-curves obtained by each of the simulators. We notice that all simulators achieve the same maximum output power. The main differences can be seen in the values of  $J_{sc}$  and  $V_{oc}$ . KASCS uses an adaptive algorithm to compute the IV-curve, while PC2D uses a fixed voltage step. Quokka has convergence issues for voltage values close to zero and use a semi-adaptive voltage step to compute the IV-curve.

## 3 Simulation results and discussion

### 3.1 Simulation parameters

All the numerical results reported hereafter were obtained using linear finite elements. The computational domain was covered by a triangulation which initially was adapted according to the variation of  $g_n$  and subsequently according to the iterates  $(\eta_\ell, u_\ell)$ , see Figure 1(right). Part of the code was developed using the *FreeFem++* finite element library, [29]. All the simulations were performed on a *Intel Xeon E5-2680 v3* workstation with 128Gb of ram running *Linux*. The iterative scheme with mesh adaptivity converges in few iterations  $1 \leq \ell_m \leq 4$  with a tolerance of  $10^{-12}$  between two successive iterates. Further, the computational time to obtain an IV-curve consisting on the average of 120 points varied

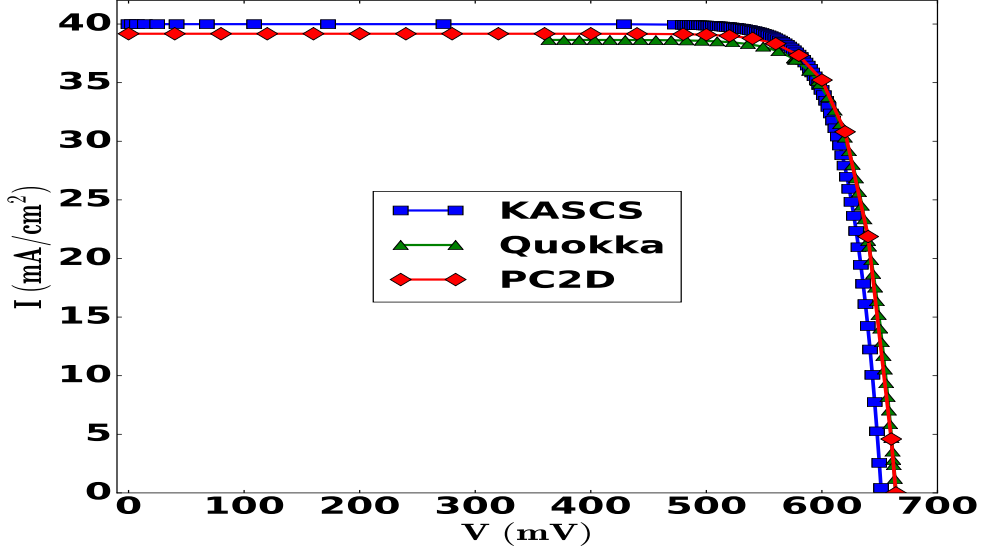


Figure 3: IV-curves comparison

from 10 – 30mns. We remark that our solver KASCS uses an adaptive algorithm to choose the voltage step in the calculation of an IV-curve.

The simulated bifacial PERC type solar cell structure is illustrated in Figure 1(left), where the emitter is covering the front surface, while the back surface is passivated and the contacts are stripe-shaped due to the considered 2D geometry. The cell base substrate is p-type with uniform doping density  $N_A = 10^{16} \text{ cm}^{-3}$ , while carrier mobility values are taken from [30],  $\mu_n = 1100 \text{ cm}^2/(\text{Vs})$ ,  $\mu_p = 427 \text{ cm}^2/(\text{Vs})$ . We also assume an ideally thin emitter covering the entire front surface, where photogeneration is occurring in the base only, while the emitter saturation current is  $J_0 = 10^{-13} \text{ A/cm}^2$ . The recombination velocity at the back passivated area is taken  $s_1 = 10 \text{ cm/s}$ , which is typical of silicon oxide or nitride passivation layers [17], while at the back contacts is calculated by the following expression  $s_2 = \frac{J_{0C} N_A}{q n_i^2}$  where  $J_{0C} = 10^{-11} \text{ A/cm}^2$  is the recombination current at the back contact. This surface recombination value corresponds to a recombination velocity within the range observed for Al-BSF laser fired contacts used in PERC solar cells [31].

The devices are considered to have zero resistive losses from the emitter, front and back contact metal grids, while shading losses of front and back fingers are assumed negligible. Light trapping is similar to the pyramidal texturing scheme, with no reflection losses from both surfaces. The impact these simplifying assumptions regarding optical losses in bifacial device efficiency is small and independent of changes in the main parameters we investigate in this work such as the back diffused contact size and base diffusion length as shown on Section 3.3. For the case of the monofacial device the back contact is considered reflective with internal reflectivity 95%. In this regard, light rays are reflected internally from the back surface and perform an additional path before exiting the cell. Since the bifacial structure is considered light transparent from both faces, we assume only one light pass from each side. The simulated front surface illumination source is the global AM1.5G spectrum [32], while the back side of the bifacial structure receives a portion of the front light, which we assume variable. We simulate three different cases of wafer thicknesses and base diffusion lengths. A wide range of back contact size widths is considered, while their spacing (pitch) is also considered as a variable parameter.

### 3.2 Device simulations and performance optimization

The simulation results presented in this section investigate the impact of geometrical parameters, back contact size ( $d$ ) and pitch ( $p$ ), to device figures of merit under various intensity levels of back illumination

as percentage  $E_{rear}$  of the direct illumination, while also considering different base material thickness ( $w$ ) and diffusion lengths ( $L_n$ ). The relative bifacial maximum power gain compared to monofacial equivalent is also evaluated.

Figure 4(left) shows the influence of illumination intensity to the back surface on the maximum output power ( $P_{max}$ ) of the bifacial simulated structures as a function of the back contact size. The relative power gain (gain factor  $GF$ ) of the bifacial structure with respect to the monofacial equivalent one (corresponding to the industrial standard Al-BSF device) is shown on the left vertical axis. Three different values of base thickness are considered, where minority carrier base diffusion length is  $200\mu m$  and back contact pitch is  $800\mu m$ . These curves show an obvious  $P_{max}$  increase when the amount of light entering the back side increased, which is more evident when irradiation intensity on the back is greater than  $200W/m^2$  ( $E_{rear} = 0.2$ ). In addition, there is a continuous gradual efficiency improvement for decreasing contact sizes, which is expected because of the reduced back surface recombination due to smaller contacting area. The reduction of base thickness also significantly improves conversion efficiency since generated carriers in the back surface can be more easily collected from the front junction. This is more evident when back light intensity is low ( $E_{rear} < 0.3$ ), where the thinnest device ( $w = 120\mu m$ ) is capable of converting more photons due to less recombination inside the bulk base material as well in the back surface due to reduced contact area. The relative power gain compared to the monofacial 2D PERC type structure (blue curve with filled circles) can be higher than 40% for the case of  $500W/m^2$  back illumination intensity, smallest back contact size and  $120\mu m$  base thickness. The power gain of the bifacial device is further increased compared to the standard 1D structure, due to the increased recombination on the back surface.

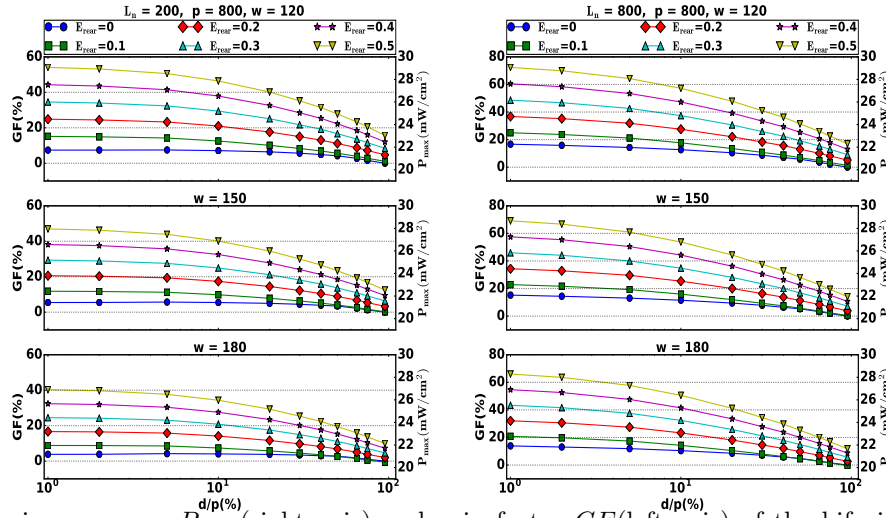


Figure 4: Maximum power  $P_{max}$  (right axis) and gain factor  $GF$  (left axis) of the bifacial device,  $p = 800\mu m$ , as a function of the ratio of back contact size to pitch size  $d/p$  (in logarithmic scale). Each curve corresponds to a different light intensity on the back surface as a portion ( $E_{rear}$ ) of the front illumination:  $E_{rear} = 0$  (circles,  $\bullet$ ),  $E_{rear} = 0.1$  (squares,  $\blacksquare$ ),  $E_{rear} = 0.2$  (diamonds,  $\blacklozenge$ ),  $E_{rear} = 0.3$  (triangles,  $\blacktriangle$ ),  $E_{rear} = 0.4$  (stars,  $\star$ ),  $E_{rear} = 0.5$  (downright triangles,  $\blacktriangledown$ ). Front illumination spectrum is AM1.5G. Each separate graph corresponds to different base thickness  $w$ . Base diffusion lengths are  $L_n = 200\mu m$  (left) and  $L_n = 800\mu m$  (right).

Figure 4(right) presents the same set of curves as before, with larger diffusion length  $L_n = 800\mu m$ . In this case, as expected the maximum power of the bifacial device is considerably improved both for all assumed cases of back illumination intensity. In contrast to Figure 4(left) however, the efficiency is not significantly improved by base thickness reduction, because in this case base carrier recombination is drastically reduced due to the much higher diffusion length. The relative maximum power gain compared to the monofacial 2D PERC type structure can be close to 50% for the case of  $500W/m^2$  back illumination, which is an indication that practically almost all of the photons generated on the back surface are successfully converted. The maximum power gain of the bifacial device is drastically improved compared to the standard 1D structure, as a result of reduced bulk and back surface recombination.



Figure 5 demonstrates the influence of back contact spacing to the maximum power of the bifacial structure as a function of back contact width to pitch ratio  $d/p$  for different back illumination intensity levels  $E_{rear} = 0.2$  and  $E_{rear} = 0.5$ , where assumed device thickness is  $180\mu m$  and diffusion length  $L_n = 200\mu m$  and  $L_n = 800\mu m$ . As the portion  $E_{rear}$  increases, the maximum power increases too and the same behaviour is observed also with diffusion length  $L_n$ .

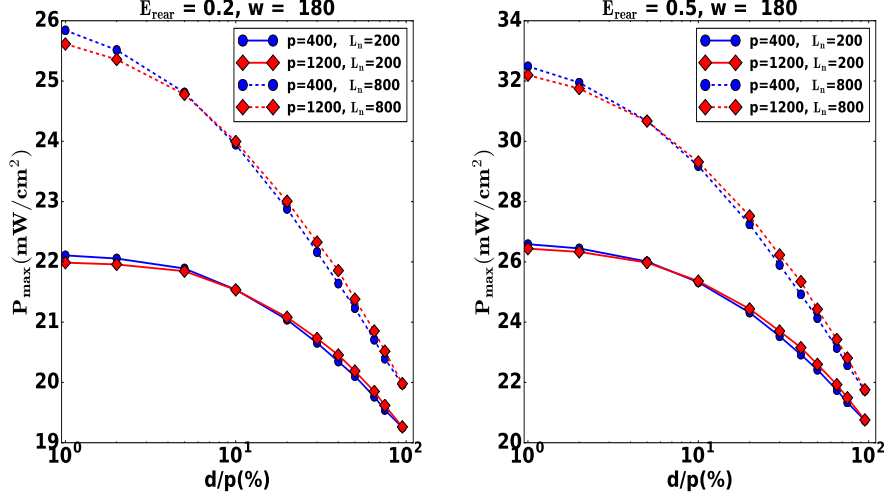


Figure 5: Maximum power  $P_{max}$  of the bifacial device of thickness  $w = 180\mu m$ , as a function of the ratio of back contact size to pitch size  $d/p$  (in logarithmic scale), assuming varying light intensities on the back surface as a portion of the front illumination with  $E_{rear} = 0.2$ (left) and  $E_{rear} = 0.5$ (right). Front illumination spectrum is *AM1.5G*. Each separate curve corresponds to different pitch size :  $p = 400\mu m$ (circles,  $\bullet$ ),  $p = 1200\mu m$ (diamonds,  $\blacklozenge$ ). Base diffusion lengths are  $L_n = 200\mu m$ (solid lines) and  $L_n = 800\mu m$ (dashed lines).

An interesting phenomenon can be observed from all four graphs: for small values of the ratio  $d/p$  a device with  $p = 400\mu m$  produces the most power, however there is a critical value of  $d/p$  where the situation is reversed and the maximum power is produced by a device with  $p = 1200\mu m$ . This could be attributed to two competing factors: On the one hand spreading resistance losses, which induce a voltage drop in the junction and are dominant in the small  $d/p$  ratios due to current crowding effects at the back contact area and on the other hand carrier recombination in the bulk base material. When back contact pitch is smaller, spreading resistance losses are reduced [33], however bulk recombination is slightly enhanced due to higher number of back contacts per unit area, which increase the carrier collection path. This critical value of  $d/p$ , depends on the diffusion length and it is  $d/p = 5\%$  for  $L_n = 200\mu m$  and  $d/p = 10\%$  for  $L_n = 800\mu m$ . Nevertheless, the difference in output power between the two devices is small. The output power of the device with  $p = 800\mu m$ (not shown in the figure) lies in between of the other two, for all values of  $E_{rear}$  and  $L_n$ . For  $d/p = 95\%$  all devices produce the same maximum power.

### 3.3 Influence of metal grid shading and surface reflection losses

In this part we investigate the impact of finger grid shading and surface reflection losses on device power output. To do so we consider two devices, one with a metallic grid on both surfaces and reflection losses, see Figure 6, and a second one without any of these losses. The size of the metallic grid is assumed to be  $100\mu m$  while the other dimensions of both devices are  $p = 1200\mu m$ ,  $w = 180\mu m$ . The contact size ( $d$ ) is taken as a percentage of the pitch size ( $p$ ). Figure 7 shows the comparison between the two devices in terms of maximum power, while the horizontal axis(in logarithmic scale) depicts the ratio  $d/p$ . The back illumination intensity fraction as a portion of the front (mixing parameter) takes values:  $E_{rear} = 0.2, 0.4$  while the base diffusion length is  $L_n = 200\mu m, 800\mu m$ . The dashed lines represent the

bifacial device with metallic grid and reflection losses, while the solid lines represent a bifacial device without any of these losses. As expected the difference in maximum power between the two devices is small, with the absolute difference(AD) never exceeding  $0.6mW/cm^2$  and the relative difference(RD) being less than 2% for all choices of mixing parameter  $E_{rear}$  and diffusion length  $L_n$ , as can be seen from Table 2. The results shown on Figure 7 and Table 2 also show that the maximum power change due to variations in back diffused contact size and base diffusion length is not influenced by grid shading and surface reflection losses.

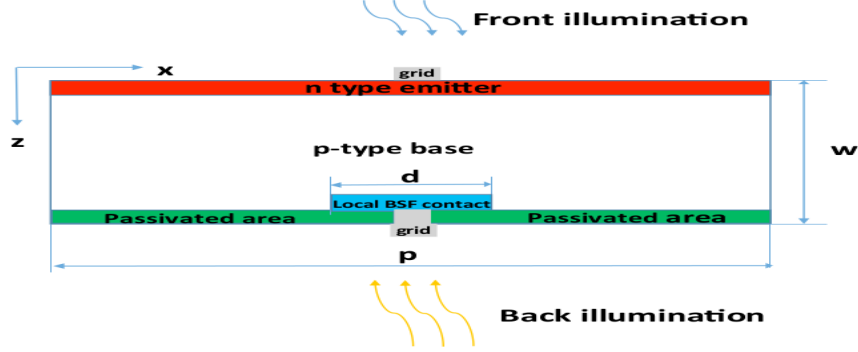


Figure 6: Bifacial solar cell with metallic grid.

$L_n$	$E_{rear} = 0.2$		$E_{rear} = 0.4$	
	AD	RD(%)	AD	RD(%)
200	0.42	1.91	0.49	1.94
800	0.50	1.94	0.59	1.98

Table 2: Absolute and relative differences in  $P_{max}(mW/cm^2)$  between the two devices.

## 4 Bifacial device performance simulation under highly diffused irradiance

This section investigates the performance of the bifacial structure during highly diffused irradiance conditions. Such conditions are very common in the Middle East region due to frequent dust storms, which introduce high levels of aerosol particles in the air. These particles scatter sunlight and change the form of the solar spectrum by significantly increasing the diffuse component of radiation while reducing the direct one. Sunlight radiation intensity at ground level is also affected depending on the sandstorm strength.

An example of such case is illustrated in Figure 8(left), where we plot the diffuse horizontal component of the solar radiation (DHI) normalized to the global one (GHI) and the Aerosol Optical Depth (AOD) at noon during the period March 17-26, 2017, where a dust storm event occurred at KAUST on March 19th. The graph shows that during the day of the dust storm the AOD level peaks at very high levels and decreases gradually, while it takes approximately one week to reach its values before the event. It is worth noting that for most of these days solar irradiance at the ground is dominated by the diffuse component, while its rate of change follows the same trend with the AOD level. On the contrary, the direct irradiance component is reduced with increasing turbidity levels as shown on Figure 8(right), which is expected since global irradiance is the sum of the diffuse and direct radiation and DHI increases proportionally with AOD as already mentioned. AOD measured values were extracted through NASA Aeronet database for the meteorological station at KAUST which is set and operated by the research team of prof. G. L. Stenchikov [34], while solar irradiance was measured through another station maintained at KAUST New

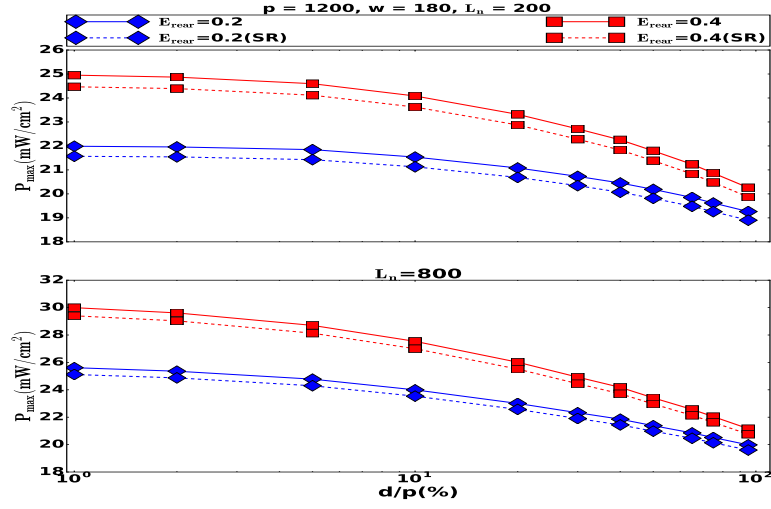


Figure 7: Comparison of maximum power between the device with grid shading and reflection losses (SR), depicted by dashed lines and a device without any such losses, depicted by solid lines as a function of the ratio  $d/p$  (in logarithmic scale). Different symbols correspond to different values of mixing parameter  $E_{rear} = 0.2$  (diamonds,  $\blacklozenge$ ) and  $E_{rear} = 0.4$  (squares,  $\blacksquare$ ).

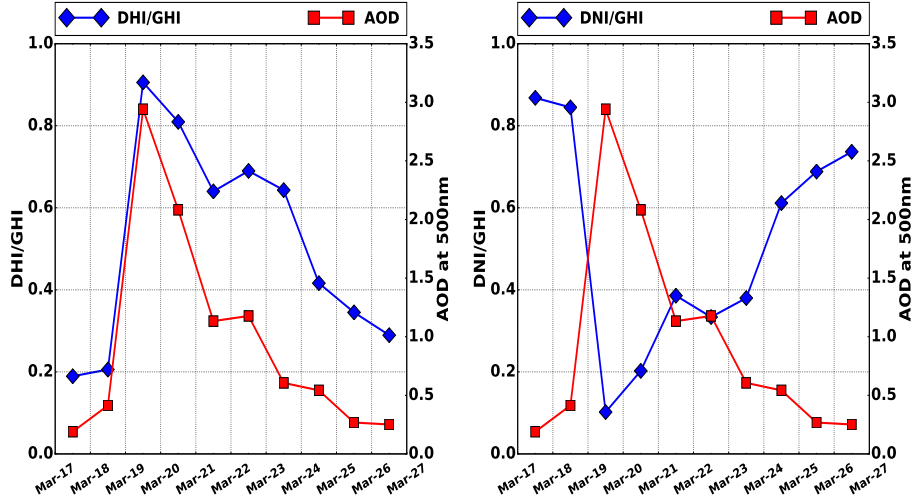


Figure 8: Diffuse (DHI) and direct (DNI) (left axis) component of the solar radiation normalized to the corresponding global one (GHI) incident at the horizontal plane in the ground and turbidity values (AOD) (right axis) for the site of KAUST in Saudi Arabia. The values were measured for the period March 17 to 26, 2017 during noon time (12:00pm).

Energy Oasis (NEO) site. It is already reported that bifacial solar modules perform significantly better compared to monofacial ones under highly diffused sunlight commonly observed in tropical climates [35] or under cloudy - foggy conditions [36], therefore we investigate by simulations if this also the case under environments with high aerosol content.

Regarding the simulation scenario we consider the location of KAUST University in Thuwal, Saudi Arabia. The front illumination of the device is the sum of the direct and diffused solar irradiance while the back side is assumed to receive all diffused and a portion  $E_{rear}$  of the direct solar irradiance :

$$G = \int \alpha(\lambda) \left( I_G e^{-\alpha(\lambda)z} + (I_{df} + E_{rear} I_{dr}) e^{-\alpha(\lambda)(w-z)} \right) d\lambda$$

where  $\alpha(\lambda)$  is the absorption coefficient at wavelength  $\lambda$  and  $I_G = I_{df} + I_{dr}$  where  $I_{df}$  and  $I_{dr}$  denote the diffused and direct solar irradiance respectively. The assumption that the whole diffused part of the solar radiation is absorbed from the back surface is based on the fact that it is independent on PV module orientation. However, in order to be effectively absorbed, the bifacial structure should be sufficiently elevated from the ground and kept in sufficient distance from the nearby modules to avoid blocking of incident light on the back side.

Using the resources of [30] we generated various solar spectrums for noon of June 21st 2016 with nine different values of the *turbidity* parameter for a device facing south at an angle of  $25^\circ$  with respect to the ground. The values of the turbidity parameter are  $AOD = 0.084, 0.25, 0.5, 0.75, 1, 1.5, 2, 2.5, 3$ . The front illumination of the device is the sum of the direct and diffused solar irradiance while the back side illumination consists of the diffused and a portion ( $E_{rear}$ ) of the direct solar irradiance. Based on the results from Section 3 we consider a bifacial device with back contact spacing  $p = 800\mu m$ , thickness  $w = 180\mu m$  and we study its maximum power output with mixing parameter  $E_{rear} = 20\%$ , two values of the ratio  $d/p = 5\%, 10\%$  and two different values of diffusion length  $L_n = 200\mu m$  and  $L_n = 800\mu m$ . The simulation results are depicted in Figure 9 where the  $P_{max}$  is shown in the left graph and the corresponding gain factor(GF), with respect to monofacial equivalent one, is shown on the right graph.

In all cases the output of the monofacial device is decreasing as the AOD factor increases. The power drop is not influenced significantly neither from the diffusion length nor from the ratio  $d/p$  and it's order of 26%, Figure 9(left). This is occurring because when AOD is increased in addition to the spectrum changes, the total intensity of the incident solar radiation is reduced. The situation is very different with the bifacial devices. In case of  $L_n = 200\mu m$  the gain factor(GF), compared the monofacial device, reaches a maximum value of about 59%, while for  $L_n = 800\mu m$  rises significantly to reach 77%, Figure 9(right).

In both cases the maximum power is achieved for the same value of the AOD parameter, namely for  $AOD = 2$ , where beyond this value, incident light intensity is significantly reduced. It is worth noting that despite the reduction of the incident incoming light due to increasing AOD values, the bifacial device performance is generally improved because of the higher diffuse component of the solar radiation which enters the back cell surface, thus compensates for this intensity reduction. The influence of the ratio  $d/p$  in the values of  $P_{max}$  varies slightly with respect to diffusion length and there is a gain of 2 – 3.5% for  $L_n = 200\mu m$  and a gain of 4 – 6% for  $L_n = 800\mu m$ . The influence of the diffusion length  $L_n$  is more evident and there is an increase of 15 – 22% in case of  $d/p = 5\%$  and 12.5 – 19% for  $d/p = 10\%$ .

## 5 Conclusions

We have presented a customized 2D model designed to simulate bifacial rear local contact PERC type PV structures in order to optimize bifacial solar cell design parameters in terms of efficiency and simulate various illumination conditions. A novel change of variables was used to transform the system of equations to a dimensionless one. The impact of finger grid shading and surface reflection losses on device power output were also investigated. The numerical solution of the transport equations for the specific geometry was obtained through the finite element method using an iterative scheme with mesh adaptivity. Our solver compares well with two well known solar cell simulators, namely Quokka and PC2D. Simulation results demonstrated that the relative maximum power gain compared to the monofacial 2D PERC type structure can be up to 59% depending on back surface illumination intensity, base substrate thickness, minority carrier diffusion length and back contact dimensions. The performance of the bifacial structure during highly diffused irradiance conditions commonly observed in the Middle East region due to high concentrations of airborne dust particles was also investigated. The simulation results showed that such

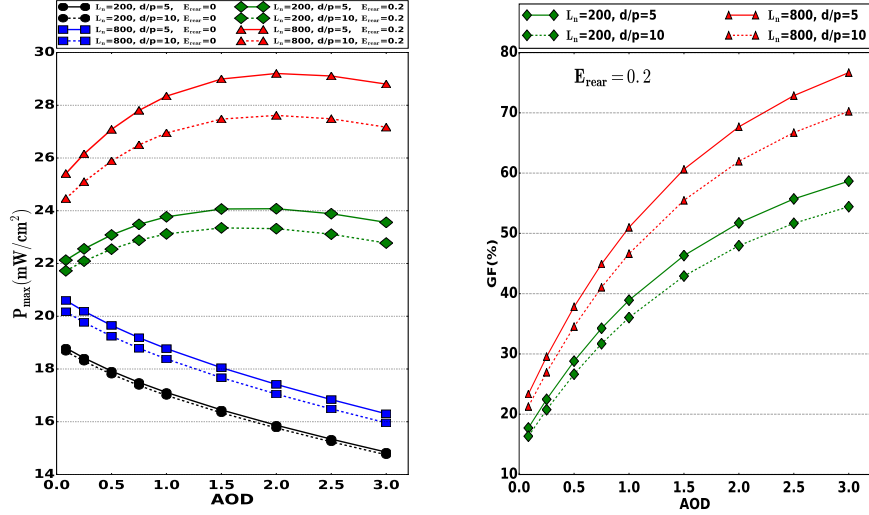


Figure 9: Maximum power  $P_{max}$ (left) and gain factor  $GF$ (right) of the bifacial device with  $p = 800\mu m$ ,  $w = 180\mu m$ , as a function of the AOD parameter, and two values of width  $d/p = 5\%$ (solid lines) and  $d/p = 10\%$ (dashed lines). **Left graph** :  $P_{max}$  for monofacial device  $E_{rear} = 0$  : circles(●) for  $L_n = 200\mu m$ , squares(■) for  $L_n = 800\mu m$  and corresponding bifacial device with  $E_{rear} = 0.2$ : diamonds(◆) for  $L_n = 200\mu m$ , triangles(▲) for  $L_n = 800\mu m$ . **Right graph** : gain factor( $GF$ ), with respect to monofacial one, of the bifacial device with  $E_{rear} = 0.2$  : diamonds(◆) for  $L_n = 200\mu m$ , triangles(▲) for  $L_n = 800\mu m$ .

conditions are favourable for the bifacial device because of the higher diffuse component of the solar radiation which enters the back cell surface. On the contrary the output of the monofacial device is negatively impacted under such conditions due to reduced intensity of incoming sunlight on the front surface. The relative maximum power gain of the bifacial device, compared to the monofacial equivalent for such conditions was up to 77% for the simulated device parameters assumed in this work.

## Acknowledgments

The authors would like to thank prof. G. L. Stenchikov of KAUST for helpful discussions regarding measurements of turbidity values and providing those data used in this work, KAUST Economic development for their support in accessing solar radiation values for the local site and Saudi Aramco R&D Center, Carbon Management Division for their support in developing this work.

## References

- [1] S. Wanga, O. Wilkieb, J. Lam, R. Steeman, W. Zhang, K-S Khoo, S-C Siong, and H. Rostan. Bifacial photovoltaic systems energy yield modelling. *Energy Procedia*, 77:428 – 433, 2015.
- [2] Y. Chieng and M.A. Green. Computer Simulation of Enhanced Output from Bifacial Photovoltaic Modules. *Progress in Photovoltaics: Research & Applications*, 1:293–299, 1993.
- [3] T. Joge, Y. Eguchi, Y. Imazu, I. Araki, T. Uematsu, and K. Matsukuma. Applications and field tests of bifacial solar modules. In *Proc. 29th IEEE PV Specialists Conference*, pages 1549–1552, 2002.
- [4] T. Warabisako, K. Matsukuma, S. Kokunai, Y. Kida, T. Uematsu, and H. Yagi. Bifacial multicrystalline Silicon solar cells. In *Proc. 23rd IEEE PV Specialists Conference*, pages 248–251, 1993.

- [5] A. Moehlecke, I. Zanesco, and A. Luque. Practical high efficiency bifacial solar cells. In *Proc. 24th IEEE PV Specialists Conference*, pages 1663–1666, 1994.
- [6] SolarWorld. SunModule, BiSun, <http://www.solarworld.de>.
- [7] Trinasolar. DUOMAXtwin, <http://www.trinasolar.com>.
- [8] Sunpreme. GxB series, <http://sunpreme.com/gxb-series-2>.
- [9] NEO Solar Power Corporation (NSP). BiFi Series, <http://www.nsp.com/s/2/product-c73729/BiFi-Bifacial-Cell.html>.
- [10] ITRPV. International Technology Roadmap for Photovoltaic Results 2016. Technical report, ITRPV, 2017.
- [11] A. W. Blakers, A. Wang, A. M. Milne, J. Zhao, and M. A. Green. 22.8 % efficient silicon solar cell. *Applied Physics Letters*, 55(13):1363, 1989.
- [12] J. Zhao, A. Wang, P. Altermatt, S. Wenham, and M.A. Green. 24efficiency silicon cell research. *Solar Energy Materials & Solar Cells*, 41-42:37–44, 1996.
- [13] Silvaco. Atlas Device Simulation Framework, <http://www.silvaco.com>.
- [14] Synopsis. Sentaurus Device, <https://www.synopsys.com>.
- [15] A. Fell. A Free and Fast Three-Dimensional/Two-Dimensional Solar Cell Simulator Featuring Conductive Boundary and Quasi-Neutrality Approximations. *IEEE Transactions on Electron Devices*, 60(2):733–738, 2016.
- [16] P. A. Basore and K. Cabanas-Holmen. PC2D: A circular-reference spreadsheet solar cell device simulator. *IEEE Journal of Photovoltaics*, 1(1):72–77, 2011.
- [17] M. Zanucoli, R. DeRose, P. Magnone, E. Sangiorgi, and C. Fiegna. Performance Analysis of Rear Point Contact Solar Cells by Three-Dimensional Numerical Simulation. *IEEE Transactions on Electron Devices*, 59(5):1311–1319, 2012.
- [18] J.M. López-González, P. Ortega I. Martín, A. Orpella, and R. Alcubilla. Numerical simulations of rear point-contacted solar cells on  $2.2\Omega\text{ cm}$  p-type c-Si substrates. *Progress in Photovoltaics*, 1:69–77, 2015.
- [19] M. Zanucoli, P. Magnone, E. Sangiorgi, and C. Fiegna. Analysis of the impact of geometrical and technological parameters on recombination losses in interdigitated back-contact solar cells. *Solar Energy*, 116:37–44, 2015.
- [20] A. Fell, K. Fong, K. R. McIntosh, E. Franklin, and A. Blakers. 3-D Simulation of Interdigitated-Back-Contact Silicon Solar Cells With Quokka Including Perimeter Losses. *IEEE Journal of Photovoltaics*, 4(4):1040–1045, 2014.
- [21] N. Wohrle, A. Sabater, and J. Greulich. Genuine bifacial simulation and optimization of an MC-Silicon PERC solar cell. In *32nd European PV Solar Energy Conference and Exhibition*, pages 1–6, 2016.
- [22] K. Krauss, F. Fertig, J. Greulich, S. Rein, and R. Preu. biPERC silicon solar cells enabling bifacial applications for industrial solar cells with passivated rear sides. *Physica status solidi. A*, 213(1):68–71, 2016.
- [23] F. Fertig, N. Wohrle, J. Greulich, K. Krauss, E. Lohmueller, S. Meier, A. Wolf, and S. Rein. Bifacial potential of single and double-sided collecting silicon solar cells. *Progress in Photovoltaics*, 24(6):818–829, 2016.
- [24] Instructions for modeling the I-V behavior of cells that are illuminated simultaneously from both front and rear surfaces.

- [25] K. Kotsovos and K. Misiakos. Three-dimensional simulation of carrier transport effects in the base of rear point contact silicon solar cells. *Journal of Applied Physics*, 89(4):2491–2496, 2001.
- [26] A. de Mari. An accurate numerical one-dimensional solution of the p-n junction under arbitrary transient conditions . *Solid State Electronics*, 11(11):1021–1053, 1968.
- [27] F. DeLa Moneda. Threshold Voltage from Numerical Solution of the Two-Dimensional MOS Transistor. *IEEE Transactions on Circuit Theory*, 20(6):666–673, 1973.
- [28] R. Bank, D. Rose, and W. Fichtner. Numerical methods for semiconductor device simulation. *SIAM J. Sci. Stat. Computing*, 4(3):416–435, 1983.
- [29] F. Hecht. New development in FreeFem++. *J. Numer. Math.*, 20:251–265, 2012.
- [30] PV-Lighthouse. <https://www.pvlighthouse.com.au>.
- [31] R. Horbelt, G. Micard, P. Keller, R. Job, G. Hahn, and B. Terheiden. Surface recombination velocity of local Al-contacts of PERC solar cells determined from LBIC measurements and 2D simulation. *Energy Procedia*, 92:82–87, 2016.
- [32] National Renewable Energy Laboratory (NREL). Reference Solar Spectral Irradiance: Air Mass 1.5, (<http://redc.nrel.gov/solar/spectra/am1.5/>).
- [33] K R Catchpole and A W Blakers. Modelling the PERC structure for industrial quality silicon. *Solar Energy Materials and Solar Cells*, 73(1):189–202, 2002.
- [34] NASA. AERONET Aerosol Robotic Network, <https://aeronet.gsfc.nasa.gov>.
- [35] J. Singh, T. Walsh, and M. Aberle. Performance investigation of bifacial PV modules in the tropics. In *Proc. 27th EUPVSEC*, pages 3263–3266, 2012.
- [36] PV-Tech, <https://www.pv-tech.org>. Are we underestimating the performance benefits of bifacial PV? , 2016.